Derivation of Multiple Co-Varying Material and Process Parameters Using Physics-Based Modeling of X-Ray Data

Gurdaman S. Khaira,[†,‡] Manolis Doxastakis,[¶] Alec Bowen,[†] Jiaxing Ren,[†] Hyo Seon Suh,[†] Tamar Segal-Peretz,[§] Xuanxuan Chen,[†] Chun Zhou,[†] Adam F. Hannon,[‖] Nicola J. Ferrier,[⊥] Venkat Vishwanath,[⊥] Daniel F. Sunday,[‖] Roel Gronheid,[#] R. Joseph Kline,[‖] Juan J. de Pablo,[*,†,⊥] and Paul F. Nealey[†,⊥]

†*Institute for Molecular Engineering, The University of Chicago, IL 60637, USA*

‡*Mentor Graphics Corporation, Wilsonville, OR 97070, USA*

¶*Department of Chemical and Biomolecular Engineering, University of Tennessee, Knoxville, Tennessee, 37996, USA*

§*Department of Chemical Engineering, Technion – Israel Institute of Technology, Haifa 32000, Israel*

‖*Material Science and Engineering Division, National Institute of Standards and Technology, Gaithersburg, MD 20899, USA*

⊥*Argonne National Laboratory, Argonne, IL 60439, USA*

#*imec, Kapeldreef 75, B-3001 Leuven, Belgium*

E-mail: depablo@uchicago.edu

Abstract

There is considerable interest in developing multi-modal characterization frameworks capable of probing critical properties of complex materials by relying on dis-

tinct, complementary methods or tools. Any such framework should maximize the amount of information that is extracted from any given experiment and should be sufficiently powerful and efficient to enable on-the-fly analysis of multiple measurements in a self-consistent manner. Such a framework is demonstrated in this work in the context of self-assembling polymeric materials, where theory and simulations provide the language to seamlessly mesh experimental data from two different scattering measurements. Specifically, the samples considered here consist of diblock copolymers (BCP) that are self-assembled on chemically nano-patterned surfaces. The copolymers microphase separate into ordered lamellae with characteristic dimensions on the scale of tens of nanometers that are perfectly aligned by the substrate over macroscopic areas. These aligned lamellar samples provide ideal standards with which to develop the formalism introduced in this work and, more generally, the concept of high-information-content, multi-modal experimentation. The outcomes of the proposed analysis are then compared to images generated by 3D scanning electron microscopy tomography, serving to validate the merit of the framework and ideas proposed here.

Introduction

Advances in synthesis and processing of materials demand that new characterization methods be developed to resolve the smallest of features of interest. As scientists and engineers continue to tighten the cycle of conception, development, and optimization, it is essential that different modes of characterization be coupled with each other through state-of-the-art theory and simulation. While the concept of combining data from complementary experiments in order to arrive at a comprehensive description of a material has been a long-standing goal of materials science and engineering, its actual implementation, particularly in the context of nanostructured polymeric materials, has been missing.

Implementing the concept outlined above requires carefully conceived standards or reference material samples for calibration of the proposed ideas. Over the last several years,

such samples have been gradually perfected in the context of nanoscale patterning with block copolymers. More specifically, the directed self-assembly (DSA) of block-copolymers (BCPs) on patterned substrates has shown significant promise as a potential bottom-up technique for development of industrial-scale lithographic processes.[1–4] Block copolymers exhibit the ability to spontaneously form periodic structures whose characteristic dimensions are in the range between 5 and 50 nm. The directed assembly of BCPs relies on external guiding fields (such as chemical patterns, topographical features, magnetic fields, voltage or shear fields) to generate perfect, defect-free morphologies over large areas, as required for commercial fabrication of electronic devices. A key concept in DSA that is of particular importance for applications and to this work is that of "density multiplication",[1,5] where a coarse guiding pattern can be printed on a substrate using conventional photo-lithography, and then used to guide the assembly of a block polymer having much smaller characteristic dimensions, thereby increasing significantly the density of relevant features (and reducing their size).

One major challenge for implementation of DSA as a patterning technique is identifying the optimal thermodynamic and guiding pattern conditions that give rise to perfect, defect-free morphology. Finding these ideal conditions requires that precise techniques be developed to characterize self-assembled BCP structures over large areas. Currently, scanning electron microscopy (SEM) is the most commonly used imaging technique for DSA characterization. Unfortunately, it only provides two-dimensional surface information. In comparison, transmission electron microscopy (TEM) does provide three-dimensional information, but it requires particularly demanding sample preparation and is limited for "in situ" characterization of structure formation. Both methods have a limited field of view and cannot probe BCP film structure over large areas.

Small angle X-Ray scattering (SAXS) techniques, primarily resonant critical-dimension small angle scattering (res-CDSAXS)[6,7] and grazing-incidence small angle scattering (GISAXS)[8] have both been used in the past to characterize BCPs. res-CDSAXS is a transmission SAXS method that uses resonant soft X-rays to enhance contrast between different BCP com-

ponents.[9] GISAXS is a reflection SAXS technique that has been used to determine the orientation and type of the block copolymer morphology in thin films. These techniques are capable of probing depth-dependent features with resolution comparable to or even finer than those accessible from top-down SEM and TEM, while illuminating a much larger region of surface area with length-scales typically in the range of hundreds of microns. However, SAXS techniques cannot pinpoint individual defects, making them complementary to real-space techniques. In the past, SAXS data have been analyzed by optimizing geometric structural models consisting of polygons to fit data.[9–13] Such an optimization procedure necessarily involves many degrees of freedom, which depend on the details of the model and the complexity of the underlying morphology.

In this work, we use a detailed model of the polymer and surface, along with res-CDSAXS and GISAXS experiments, to determine the morphology of lamella-forming polystyrene-*b*-poly-methylmethacrylate (PS-*b*-PMMA) BCPs on a chemical pattern. Industrial applications of this process include, for example, generating lines and spaces for FinFET manufacturing.[14,15] Without loss of generality, we focus on chemical patterns fabricated by the so-called LiNe flow,[16–18] which has been extensively optimized for first generation materials such as PS-*b*-PMMA. A schematic representation of the chemical pattern formed by this process is shown in Fig. 1a. Crosslinked polystyrene (XPS) guiding stripes of specific width (W) and pitch are fabricated on the substrate using conventional photo-lithography and oxygen-plasma etch. The isotropy of the etch process results in tapered, rather than perpendicular, sidewalls. Williamson et al[19] found that during the etch process, the XPS sidewall is oxidized due to exposure to plasma, making the XPS sidewall PMMA preferential as opposed to the unexposed XPS top which remains PS preferential. The remaining substrate area is grafted by a random PS-*r*-PMMA brush whose chemistry can be tuned based on the required degree of density multiplication.[17,20] As is evident from Fig. 1a, there is a multitude of synthesis and processing parameters whose effect on pattern fidelity has to be quantified in order to extract a working recipe. Developing schemes to produce defect-free

morphologies is part of an extensive ongoing effort in making the transition from the laboratory to industrial fabrication facilities. It is precisely in this step where the synergy of theory-modeling and experiments could have a significant impact.

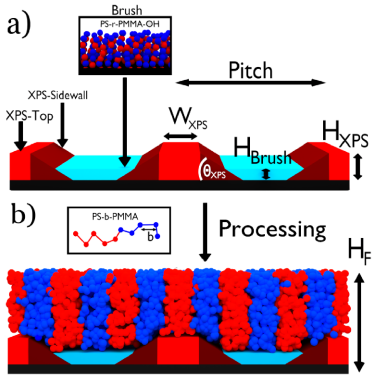

Figure 1: **Schematic of Directed Self-Assembly.** 3X density multiplication of PS-PMMA block copolymer on chemical patterns fabricated by the LiNe flow.[17]

We rely on a Theoretically Informed Coarse-Grained (TICG) Model which has been extensively used in the past to simulate the self-assembly of BCPs with excellent agreement to experimental data.[21–23] This model uses a well-established polymer theory[24,25] to describe BCP molecular interactions and therefore provides a consistent representation of BCP morphology given a small number of input parameters. We use experimental X-ray scattering data to determine the optimal thermodynamics and chemical pattern input for our molecular simulations. Optimization of these input parameters is driven by an evolutionary algorithm called covariance matrix adaptation evolutionary strategy (CMA-ES), which has been shown in the past to be an efficient scheme for optimizing the DSA process.[20,26–28] Once optimization is complete, the BCP morphology obtained from these input parameters is shown to reproduce the major features in scattering profiles acquired by X-ray experiments. The validity of the structures determined from these scattering techniques is confirmed by direct comparison to results from 3D scanning TEM (STEM) tomography.

In the past, atomistic simulations have been used to investigate SAXS experiments of biomaterials.[29] These methods have been used to calculate 1-dimensional scattering curves from non-periodic molecular structures. In comparison, our system is periodic, which allows

it to provide substantially more scattering information, and the material density is treated as a continuum over hundreds of nanometers, which allows for more detailed and accurate fits. A key feature of this work is that it provides a first example of a full metrology that combines complementary experimental data samples to arrive at material parameters clearly defined within a reliable physical model of the system. The successful application of the proposed methodology does not only allow one to determine a film morphology that is consistent with SAXS characterization, but it also provides unique information on the molecular driving forces that lead to the observed structures, thereby turning modeling into a predictive tool. We anticipate that applications of the approach espoused here will provide the means to leap forward in developing new materials and processes that are able to meet stringent industrial requirements for application of DSA in commercial processes.

Results and Discussion

Scattering Model

The model parameters that are optimized when fitting experimental scattering data are displayed in Fig. 1. They can be classified into two categories, namely system geometry and thermodynamic material properties. The geometry of the thin polymer film is defined by 1) the total height of the film above the substrate (H_{F}, determined by reflectivity experiments to be in the range of 42-43 nm), 2) the height of the XPS guiding stripe (H_{XPS}), 3) the side-wall angle of the guiding stripe with the substrate (θ_{XPS}), 4) the height of the neutral brush (H_{Brush}) and 5) the top-width of the XPS guiding stripe (W_{XPS}). The material-specific thermodynamic parameters include three polymer-polymer and polymer-substrate interaction parameters: χN_{SM} (between PS and PMMA segments), χ_{XS-S} (between guiding stripe sidewall and PS), and χ_{B-M} (between backfill brush and PMMA). These parameters are used within the TICG Model to generate a statistical ensemble of density fields from which a scattering pattern is calculated. In our calculations, an ensemble of structures that

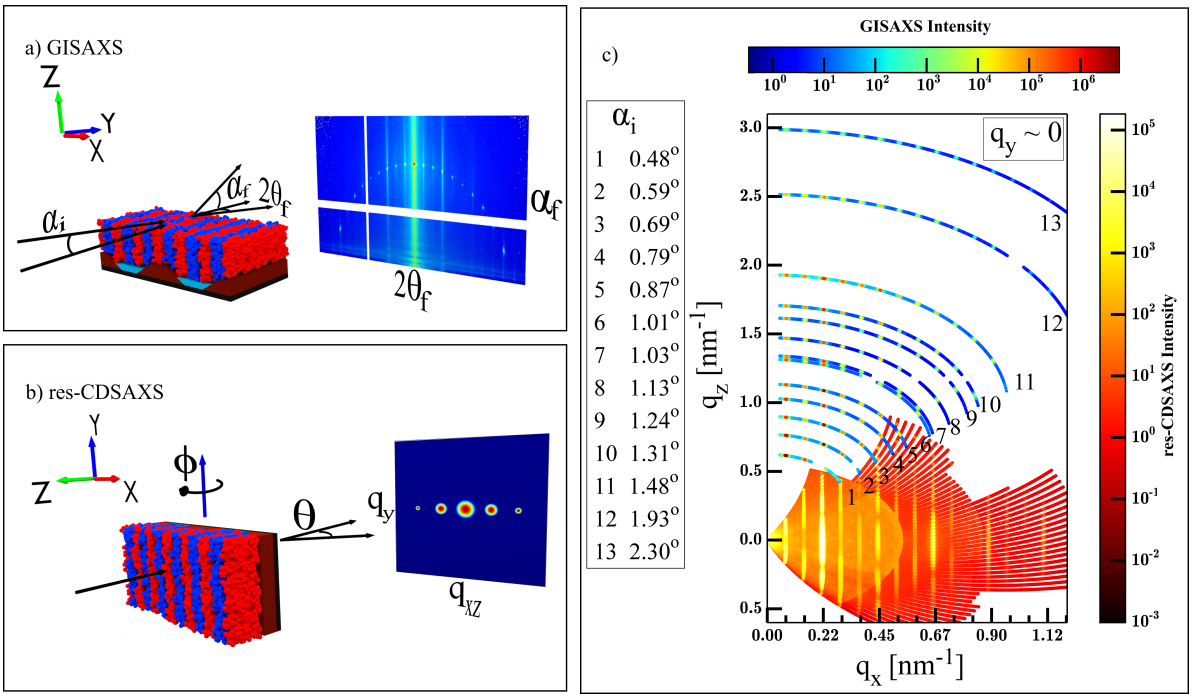

Figure 2: **Comparison of GISAXS and res-CDSAXS experiments.** Schematic of X-ray scattering of BCP thin films using **a**, GISAXS and **b**, res-CDSAXS. **c**, Structural information obtained from X-ray scattering in the inverse space for sample W093. Note that in all scattering experiments the x-axis is defined as normal to the oriented polymer lamella, which is standard practice for res-CDSAXS, but non-standard for GISAXS.

are typically very rough and asymmetric (exhibiting properties such as line edge roughness) are converted to binary density fields (PMMA-poor and PMMA-rich domains). The PMMA-rich domains are described by a sum of polygonal shape functions with an analytic Fourier transform $\hat{\rho}(\mathbf{q})$ [30] and a smoothing function introduced in inverse space to account for the inherently diffuse polymer interfaces. The X-ray scattered intensity can be described as:

$$I(\mathbf{q}) = I_m(\mathbf{q}) + I_d(\mathbf{q}) = |\langle\hat{\rho}(\mathbf{q})\rangle|^2 + \langle|\hat{\rho}(\mathbf{q}) - \langle\hat{\rho}(\mathbf{q})\rangle|^2\rangle \quad (1)$$

where $\hat{\rho}(\mathbf{q})$ is the scattering amplitude as a function of inverse space coordinates $\mathbf{q}$. I_m represents the main scattering compared to calculations while I_d represents the diffuse scattering. The use of soft X-rays near an absorption edge allows res-CDSAXS to greatly enhance the scattering contrast between domains, while the large volume probed by hard X-rays at a grazing incidence angle allows GISAXS to examine the electron density contrast between domains. In the case of res-CDSAXS, calculations are performed within the Simple Born Approximation (SBA) while the Distorted Wave Born Approximation (DWBA) is used for GISAXS [8,12,31–34] to compute I_m from simulations and compare to experimentally recorded data. The weak contributions from the brush (cyan domains in Fig. 1) to the scattering are added with half the weight to account for the corresponding PMMA composition.

For res-CDSAXS analysis, we only fit the scattered intensity as a function of q_z along the peaks located at discrete values of $q_x = 2\pi n/84$ nm^{-1} associated with the substrate pattern periodicity. At these peaks, the contribution of the diffuse scattering (second term in Eq. 1) is negligible and approximated with a constant background. For GISAXS the intensity is recorded in arcs shown in Fig. 2, each of them corresponding to different incidence angles (α_i). [35–39] Along these arcs, both q_x and q_z vary continuously and simultaneously according to relationships that are described in the literature. [12,31] The range of GISAXS incidence angles above the critical angle was selected on the basis of the following criteria: first, incidence angles above the critical angle distribute the electric field more uniformly throughout the polymer film. As the incidence angle approaches the critical angle, the

scattering becomes increasingly surface sensitive and highly dependent on the topography of the polymer-air surface. In our analysis, the internal morphology is more important to our aims of understanding the polymer-polymer and polymer-template interactions than the structure of the polymer-air surface. Second, higher incidence angles correspond to details on a smaller scale in reciprocal space, and therefore provide the resolution necessary to understand the finer features of the polymer morphology that are of interest to this study.

Model Fits

In this study, we considered five separate samples that differ solely in the underlying chemical guiding pattern geometry. Samples are labeled according to their ratio of guiding stripe width to the natural polymer periodicity (i.e. W047 is a sample with $W/L_0 = 0.47$) and are all based on 3X density multiplication. An initial estimate of the pattern geometric parameters was determined on the basis of SEM imaging. All model parameters were optimized using CMA-ES by directly comparing simulation predicted res-CDSAXS scattering profiles to experimentally recorded res-CDSAXS spectra. Simulated GISAXS spectra were calculated using these optimized model parameters. An example scattering comparison using optimized parameters for a sample (W093) with expected $W/L_0 = 0.93$ is shown in Fig. 3b and 3d. The corresponding resulting morphology for this sample is shown in Fig. 4a. The res-CDSAXS scattering profiles can be decomposed into two distinct categories: the five high-intensity polymer Bragg peaks (second, fifth, eighth, eleventh, and fourteenth peaks), which correspond to the natural spacing of the polymer, and the lower-intensity template super-lattice Bragg peaks, which correspond to the pattern template spacing. The polymer Bragg peaks largely account for the polymer morphology, and contain information about polymer interface widths and interface fluctuations. The template super-lattice Bragg peaks account for features that do not have the same periodicity as the polymer, such as template geometry, or polymer-surface interactions. Additionally, the template super-lattice Bragg peaks are more sensitive to the assumptions made in the model, such as the air-polymer

interface being flat. The res-CDSAXS results from simulation and scattering are in good agreement for all Bragg peaks, particularly when considering the small number of optimization parameters. While slight discrepancies are apparent in the lower intensity super-lattice Bragg peaks, the fitting is particularly satisfactory for the polymer Bragg peaks, which contain more of the statistical and thermodynamic polymer information. Our simulations are able to reproduce the experimental GISAXS spectra for incidence angles α_i ranging from 0.48° to 1.31^o with satisfactory accuracy. The comparison to experimental data becomes less favorable at high exit angles ($\alpha > 1.31°$), where GISAXS is capable of probing structures at higher resolutions than the model employed in our simulations (3.19 nm). Nevertheless, the minimal number of optimization parameters and the physical description of the density fields by simulations allows for an unparalleled self-consistent description of our scattering profiles as evidenced by the extracted data.

The final set of simulation parameters for the five samples are shown under two different optimization conditions in Fig. 3a. The first set (in red) corresponds to an optimization in which each sample was treated independently. We found that optimizing the parameters independently for each sample often led to different values for thermodynamic material constants (such as χN_{SM}) as some simulation parameters have a stronger effect on the resulting intensity pattern than others. Therefore, the second set (in blue) is the result of imposing thermodynamic material constants to be identical (adopted from the fits for sample W093) across all five samples and optimizing the geometric parameters independently. The resulting predicted scattering spectra under these constraints remain in good agreement to experimental data (W066, W073, and W114 are displayed in Supporting Figure 3). This approach (holding the thermodynamic material properties constant across all samples) exemplifies the level of self-consistency in sample characterization that can only be achieved using established molecular simulation models.

For a narrower guiding stripe (W047) below half L_0, one can appreciate that the PMMA domains curve towards the sidewall of the guiding stripe, as the PS is tightly held by the

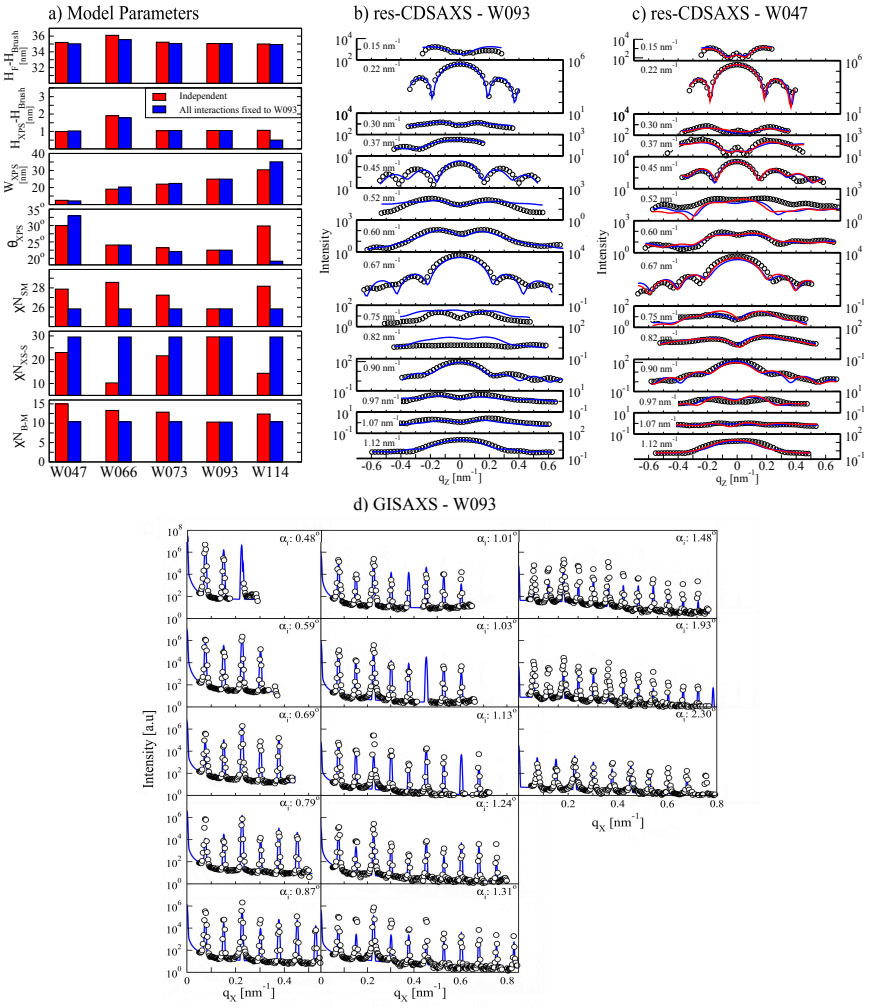

Figure 3: **Optimized simulation parameters and comparison of experimental and simulated scattering spectra.** **a**, Optimized thermodynamic and geometric parameters for all samples. Red bars are results when parameters for all samples were optimized independently. Blue bars are results when the thermodynamic interaction parameters were constrained to those of sample W093. **b**, res-CDSAXS spectra for a sample with $W/L_0 = 0.93$. Black circles are experimental data, while blue lines are predictions based on an independent simulation fit. **c**, res-CDSAXS spectra for sample with $W/L_0 = 0.47$. Red lines are predictions based on an independent simulation fit, while blue lines are predictions when the thermodynamic interaction parameters are constrained to match those of sample W093. **d**, GISAXS spectra for sample with $W/L_0 = 0.93$. GISAXS spectra was calculated using the morphology from the independent res-CDSAXS fit.

XPS. As W_{XPS} increases, the width of the PS domain near the XPS-Top increases and the PMMA domains begin to curve away from the guiding stripe. The PMMA curvature changes again towards the guiding stripe for W114, where a single PMMA domain is centered over the guiding stripe, similar to the 1.5 L_0 guiding pattern.[20]

From Fig. 3, one can see that χN_{SM}=25.8 (χN_{eff}=17) describes the experimental data from both scattering techniques. For PS-PMMA of molecular weight 21k-21k, this value corresponds to an effective temperature of 38 °C,[40] which supports that the structure of the self-assembled morphology corresponds to an effective temperature that is much lower than the annealing temperature. The XPS sidewalls appear to be strongly preferential to PMMA ($\chi N_{XS\text{-}S}$=29.6, $\chi N_{XS\text{-}M}$=0). This latter feature represents a non-trivial observation that arises naturally from our analysis, and that is also quantitatively consistent with recent findings pertaining to the three-toned nature of the underlying patterns that may arise in the LiNe process.[19]

Another interesting feature about the resulting morphologies in Fig. 4a is that they all indicate that the brush is slightly preferential to PS. The brush used in sample preparation consists of PS-r-PMMA with 51 % PS by volume fraction, a polymer that is expected to exhibit an overall neutral interaction towards PS and PMMA.[17] This result is counter-intuitive; however, upon further investigation of the structure with STEM imaging, as shown in Fig. 6, it can be confirmed that the PMMA blocks are broken by multiple discontinuous PS sections near the interface between the polymer and brush. Williamson and coworkers found similar discontinuous PMMA domains over the brush for similar chemical patterns.[19] They attributed such effects to the formation of PS microbridges, which effectively reduce the depth of the PMMA domain over the brush. As such, these breaks in the PMMA domains occur due to a slight PS preference within our simulation model. We emphasize that each morphology presented in Fig. 4a represents an average over the y-direction exactly as the high intensity spots recorded in detector images shown in Fig. 2a, 2b collapse information at inverse-space coordinates of $q_y \approx 0$. However, even for similar two-dimensional density

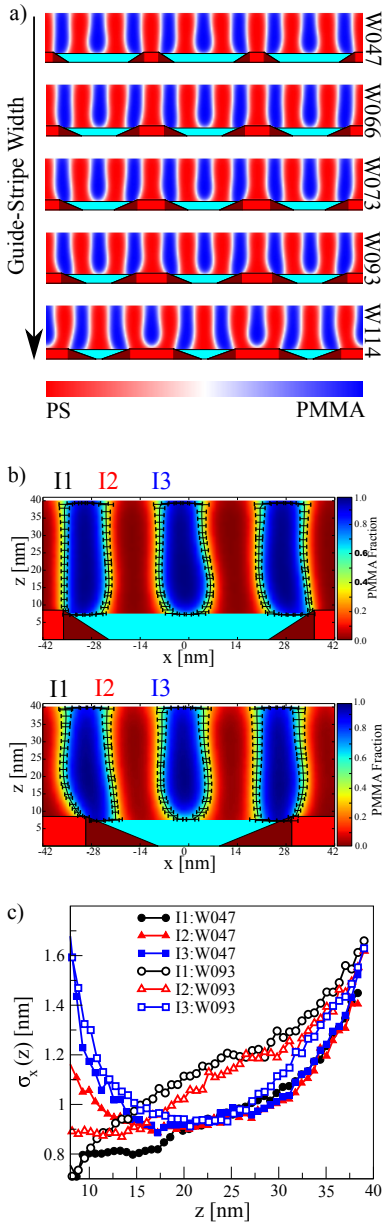

Figure 4: **Simulated morphologies and line edge roughness analysis. a**, Final morphologies fitted to scattering data from five separate samples. Individual scattering spectra for each sample is provided in supporting information. **b**, Examination of structural fluctuations in the film as a function of location over pattern. Error bars represent the standard deviation of the center of the interface throughout the film. **c**, Standard deviation of interface location as a function of film depth. This standard deviation value is a measure of line edge roughness.

profiles, distinct positional fluctuations of the interfaces (termed commonly as line edge roughness, LER) can be revealed through a detailed analysis of molecular simulation data.

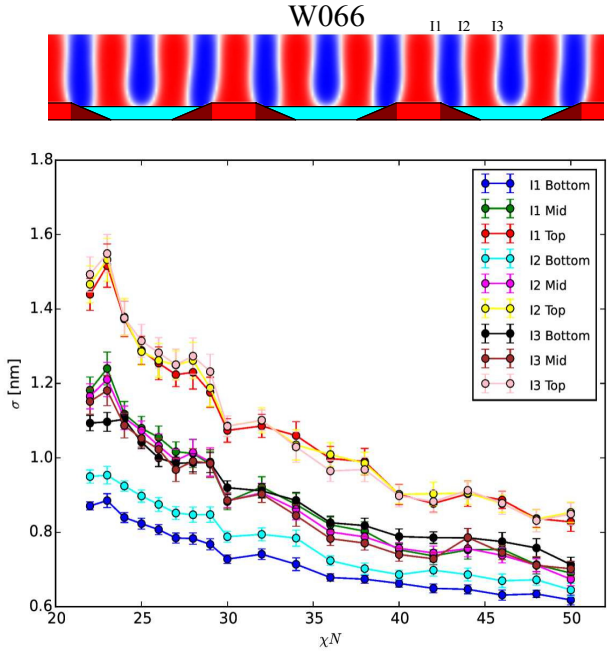

Figure 5: **Line edge roughness dependence on Flory Huggins χN parameter.** Interface fluctuation predictions for sample W066. All curves are for the chemical pattern as determined through SAXS fittings, but with the block copolymer χN varying. All three unique interfaces are plotted separately for fluctuations near the top, middle, and bottom of the film.

Interfaces and Line Edge Roughness

The statistical ensemble of density fields used to calculate the scattering profiles can also be used to examine contributions to the average interfacial width describing the gradual density changes across the PS-PMMA boundaries. Following past studies,[10] the apparent interfacial width from our scattering data (dictating to a large extent the intensity loss along q_x) is attributed to both a distribution of segments around the center of the interface as well as positional fluctuations of a fictitious PS-PMMA sharp boundary. While res-CDSAXS or GISAXS experiments can be used to determine roughness for systems with sharp interfaces, they alone do not provide sufficient information to determine the individual contributions of

the diffuse interface and structural fluctuations to the scattering.[13] However, by supplementing our measurements with the results of the TICG model, which incorporates fluctuations explicitly, the two contributors to the apparent interfacial width can be decoupled, and one can examine how the magnitude of fluctuations is affected by the pattern and the rest of the film. In particular, by examining the standard deviation of the center of the PS-PMMA interface as a function of height, we can investigate the dependence of line edge roughness (LER) on film depth and location over the chemical pattern. Fig. 4b presents two example morphologies along with standard deviations of interface location as a function of film height. Note, that while the average morphology between the two samples appears similar, interfacial fluctuations, as a function of film depth shown in the graph in Fig. 4c present significant differences. For sample W093, shown in Fig. 4b, there are three distinct types of PS-PMMA interfaces relative to the location over the chemical pattern: the interface between the XPS top and sidewall (I1), between the XPS sidewall and brush (I2), and over the center of the brush (I3). Due to the effects of the chemical pattern, the LER shows different dependence on film depth for each of these interface types. The LER of all interface types behaves similarly near the top of the film where the pattern effects are less pronounced. At the bottom of the film, interfaces near the guiding stripe are anchored more strongly and LER decreases, while interfaces over the brush have high LER near the bottom of the film with a minimum LER in the middle of the film. These results underline the need to account for non-uniform fluctuations throughout the polymer film in the analysis of experimental data, a feature which has been largely overlooked in the past.

Beyond analysis of existing data, the TICG model, calibrated from SAXS profiles, was used to investigate and predict the magnitude of interface fluctuations as a function of material properties. Block copolymers with χN values between 20-50 were simulated on the five substrate patterns. Figure 5 shows the results for these calculations for sample W066. The trends in interface fluctuations were calculated as a function of χN for the three unique interface types in the film (I1, I2, and I3) at different depths. The results show that the

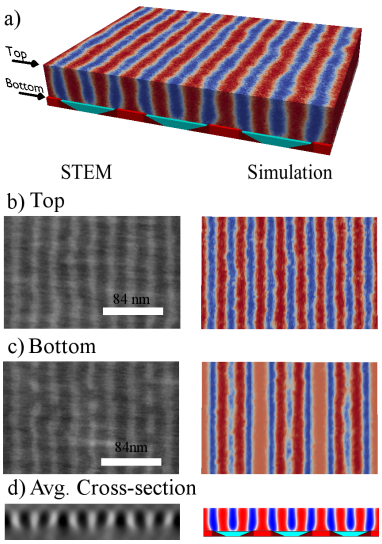

Figure 6: **Comparison of STEM Tomography to simulated scattering derived morphology.** **a**, Three dimensional BCP morphology obtained by using CMA-ES optimized pattern parameters for sample W093. Comparison of the STEM with the simulation predictions at **b**, Top of the film, **c**, Close to the pattern (bottom) and **d**, average cross-sections. In STEM, PS and PMMA domains are dark and light respectively, while they are red and blue respectively in the simulations.

interface fluctuation behavior at the top of the film and the middle of the film is nearly independent of location over the guiding pattern, and the dependence on χN is identical. At the bottom of the film, however, fluctuation behavior depends heavily on the guiding pattern. Interfaces that are located between the PS-preferential guiding stripe and PMMA-preferential sidewall (I1) are anchored strongly in place, and have a weaker dependence on χN. Those located over the brush (I2 and I3) are less strongly anchored and have similar behavior to the interface near the top or middle of the film. The highest magnitude fluctuation behavior appears to occur in regions with high curvature. For example, the interface located over the guiding stripe in sample W114 (I1, shown in the Supporting Information) has a weaker dependence on χN and greater fluctuations at high χN than any other interface.

Conclusion

A new characterization framework has been introduced by combining physics-based models and different experimental scattering techniques capable of probing the complex, hierarchical structures commonly found in ordered materials. For the particular example considered here, namely that of a self-assembled polymer film on a nano-patterned substrate, it is not only capable of characterizing the average morphology of the material, but it also furnishes thermodynamic information that is otherwise unavailable in a manner pertinent to a molecular model. This thermodynamic information can serve to better clarify which of the numerous process conditions must be adjusted to achieve a desirable, defect-free morphology. Our belief is that such a method can advance our knowledge of these materials to the point where significant progress can be made in applying them to large-scale industrial processes, and, more generally, to wide classes of materials.

Further research will expand the proposed methodology to incorporate the full three-dimensional scattering. Currently, our analysis only uses scattering along a single plane (q_x-q_z where $q_y = 0$), where all the q_y information has been integrated over. While the scattering from this plane is indispensable for describing the average structure in the x-z plane (as shown in Fig. 4a) and standard deviations for LER (Fig. 4b and 4c), directly using all three dimensions of the available scattering data, rather than just two, will allow us to determine characteristic length-scales in the y-direction, such as correlation lengths for line edge roughness. Fig. 6 compares an experimental image produced via STEM tomography to its corresponding simulated image along the y-direction after fitting to SAXS data. By incorporating out-of-plane scattering into the model, it will be possible to characterize the full three-dimensional structure, thereby enhancing the capabilities of high-throughput X-ray based metrology.

Methods

Experimental Methods

Sample Description: DSA was performed using the 300 mm wafer processing line at IMEC in Leuven, Belgium, following previously reported methods.[18] An XPS layer of thickness 8 nm was coated onto the substrate and annealed for crosslinking. The XPS was patterned with immersion lithography and O_2 plasma into line and space patterns consisting of unexposed XPS guide stripes and exposed background regions. The pitch of the guide stripes was 84 nm and the width W_{XPS} was systematically varied between different samples. A random copolymer brush was then coated on the pattern and annealed. The brush was mainly grafted to the background region to a thickness of 7 nm and the excess material was then thoroughly rinsed off. A 35 nm thick film of lamellar forming PS-b-PMMA (L_0 = 28 nm) was spin coated onto the chemically patterned substrates and then annealed at 250°C for 5 minutes under N_2 to self-assemble. W_{XPS} for all samples was measured by SEM imaging before resist removal and the average θ_{XPS} for samples with similar geometry was measured via GISAXS.[19] The summary of the geometry measurements is given in Supporting Table 1.

STEM Tomography: The three dimensional structure of DSA films was characterized using scanning transmission electron microscopy (STEM) tomography. To enhance the contrast between the blocks, selective growth of Al_2O_3 in the PMMA domains was used to stain the PMMA domains.[41–43] Thus, bright domains in STEM images correspond to PMMA domains stained with Al_2O_3, while dark domains correspond to PS domains. A series of 51 STEM images (with 30 second acquisition time per image) were acquired at tilt angles ranging from $-68°$ to $68°$, followed by alignment and reconstruction to obtain reconstructed volume of the DSA film, with dimensions of 0.5 μm $\times$ 0.5 μm $\times$ 0.01 μm (x,y,z).

GISAXS: GISAXS experiments were performed at Sector 8-ID-E in the Advanced Photon Source at Argonne National Laboratory,[44] following the procedure described elsewhere.[12,13] Each sample, originally prepared on a 300 mm wafer, was cleaved into an ap-

proximately 7.5 mm by 5 mm (x versus y) size piece fully covered by the DSA sample. The samples were measured under vacuum with an incident X-ray beam of 7.35 keV (λ=0.1687 nm). The X-ray beam was 20 μm in height and 200 μm in width. The samples were carefully aligned for azimuthal rotation angle, defined as the angle between incident X-ray beam and the direction of X-PS guide stripes, to be zero. Scattering images at different incident angles ranging from 0.46° to 2.3° were collected. The sample-to-detector distance (SDD) was set as 2157 mm for incident angles above 1.4° and 1304 mm for incident angles below 1.4°. A fresh area was exposed to the X-ray for each incident angle. Each GISAXS pattern was the result of summing 90 and 300 images of 1 second exposure scans for data collected at longer and shorter SDD, respectively. In order to minimize the radiation damage on BCP samples, the samples were exposed to the beam for 1 second at every 4 seconds. Before analysis of GISAXS data, the incident angles were calibrated based on SDD, the position of the direct beam, and the specular point shown in the GISAXS patterns at $\alpha_i = \alpha_f$ and $2\theta_f = 0$.

res-CDSAXS: res-CDSAXS using soft X-ray characterization in transmission geometry required the BCP film to be placed on thin membrane substrates. A back etch method was employed to fabricate the membrane in-situ after DSA.[45] Before DSA, SiN_x layers were deposited onto both sides of the substrate. DSA was then performed on the front side of the wafer. After DSA, the wafer was segmented into coupons and a rectangular area of nitride on the back side was removed using mechanical scribing. The coupon was then placed in a holder that sealed off and protected the polymer side while exposing only the back-side nitride pattern. The setup was immersed in potassium hydroxide solution to completely etch the exposed Si until reaching the nitride layer on the front side. The resulting nitride membrane had a thickness of 13 nm and a size of 0.9 mm 2.2 mm to allow ±70° of maximum tilt angle.

The soft X-ray res-CDSAXS experiments were performed at beamline 11.0.1.2 at the Advanced Light Source in Berkeley, using the procedure developed by Kline and co-workers.[9] The scattering vector was first calibrated with a grating sample of known pitch. The sample

chamber was kept under high vacuum ($< 10^{-5}$ Pa) and the X-ray energy was set to 282 eV near the carbon absorption edge to enhance the contrast between PS and PMMA while avoiding extensive beam damage. The beam was circular and the spot size was approximately 300 μm. The membrane sample was measured in transmission geometry and rotated from -70° to 60° with increments of 1°. The axis of rotation was parallel to the DSA line patterns. Collection time varied from 0.1 to 60 s depending on the rotation angles to maximize the signal-to-noise ratio.

Computer Simulations

The TICG model used in this study has been described extensively in the literature.[21] Here we include only the details necessary to simulate our system of interest: a three-tone chemical pattern. The system Hamiltonian can be broken into two terms: the bonded energy describing short range interactions along the polymer backbone and the non-bonded energy describing long-range intermolecular interactions. The bonded energy is shown in Eq.2.

$$\frac{H_b}{k_B T} = \frac{3}{2b^2} \sum_{J=1}^{n} \sum_{K=1}^{N-1} (\mathbf{r}_{K+1}^J - \mathbf{r}_K^J)^2, \tag{2}$$

where $\mathbf{r}_K^J$ is the position of the K^{th} segment of chain J.

The non-bonded contribution to the Hamiltonian is modified to include substrate interaction effects, unlike previous work .[17,21,22] The local densities of PS and PMMA are denoted by $\phi_S(\mathbf{r})$ and $\phi_0 M(\mathbf{r})$ respectively. The chemical pattern is modeled by three additional components, $\phi_{XT}(\mathbf{r})$, $\phi_{XS}(\mathbf{r})$ and $\phi_B(\mathbf{r})$ representing the density of XPS-Top, XPS-Sidewall and brush respectively. Unlike the copolymer which is evolved during the simulation, these materials are modeled as constant fields constrained within the substrate geometry. The contribution to the inter-molecular, or non-bonded, interactions (H_{nb}) of the aforementioned

species is given by:

$$\frac{H_{nb}}{k_BT} = \frac{\sqrt{\bar{N}}}{R_e^3}\int_V d\mathbf{r}(\sum_{\alpha,\beta}\chi N_{\alpha\beta}\phi_\alpha(\mathbf{r})\phi_\beta(\mathbf{r}) + \frac{\kappa N}{2}(1-\sum_\alpha \phi_\alpha(\mathbf{r}))^2), \tag{3}$$

where α, β any of PS, PMMA, XPS-Top, XPS-Sidewall, Brush. The sum $\sum_{\alpha,\beta}$, represents all the possible unique permutations of α and β such that $\chi \mathrm{N}_{\alpha\beta} \neq 0$. $\sqrt{\bar{N}}$ is the interdigitation number, a measure of the number of polymer chains each chain interacts with. All polymer-polymer and polymer-substrate interactions are described by a Flory-like parameter.

The interaction of XPS-Top with PS and PMMA is treated the same as PS with PS and PS with PMMA ($\chi \mathrm{N}_{\mathrm{SM}}$), respectively. Additionally, the substrate interaction differences between PS and PMMA, $\chi N_{XS-S} - \chi N_{XS-M}$ and $\chi N_{B-M} - \chi N_{B-S}$, better describe the polymer-substrate interactions than the absolute values of χN_{XS-S}, χN_{XS-M}, χN_{B-M} and χN_{B-S}. Hence, we set $\chi N_{XS-M} = \chi N_{B-S} = 0$. These interaction parameters are shown in Supporting Table 2.

Simulations were equilibrated using $\sqrt{\bar{N}}$=83, R_e = 17.75 nm, χN_{SM}=22 and κN=23. These correspond to a PS-PMMA copolymer with a molecular weight of 22K-22K g/mol and a natural periodicity of 28nm when annealed at 250°C.

Scattering Calculations

The scattering intensity from a general DSA film with scattering density $\rho(\mathbf{r})$ can be calculated as

$$I(\mathbf{q}) = |\hat{\rho}(\mathbf{q})|^2 \tag{4}$$

where $\hat{\rho}(\mathbf{q})$ is the complex scattering amplitude. For res-CDSAXS experiments, the simple Born Approximation is sufficient, and $\hat{\rho}(\mathbf{q})$ can be calculated directly as the Fourier transform of $\rho(\mathbf{r})$:

$$\hat{\rho}(\mathbf{q}) = \mathscr{F}[\rho] \tag{5}$$

In GISAXS experiments, $\hat{\rho}(\mathbf{q})$ must be calculated within the Distorted Wave Born Approximation (DWBA) to account for multiple scattering effects and refraction within the polymer film:[8,13]

$$\begin{aligned}\hat{\rho}(\mathbf{q}) =& \hat{\rho}(q_x, q_y, k_z^i, k_z^f) \\ =& T(\alpha_i)T(\alpha_f)\mathscr{F}[\rho](q_x, q_y, k_z^f - k_z^i) \\ &+ R(\alpha_i)T(\alpha_f)\mathscr{F}[\rho](q_x, q_y, k_z^f + k_z^i) \\ &+ T(\alpha_i)R(\alpha_f)\mathscr{F}[\rho](q_x, q_y, -k_z^f - k_z^i) \\ &+ R(\alpha_i)R(\alpha_f)\mathscr{F}[\rho](q_x, q_y, -k_z^f + k_z^i)\end{aligned} \tag{6}$$

where α_i and α_f are the incident and exit angles, and T and R are the Fresnel transmittance and reflectance. These four terms account for single scattering and three types of multiple scattering effects. We implement both the Simple Born Approximation and Distorted Wave Born Approximation calculations by treating the scattering density as a sum over a collection of shapes

$$\hat{\rho}(\mathbf{q}) = \sum_J F_J(\mathbf{q})\exp(i\mathbf{q}\cdot\mathbf{r}) \tag{7}$$

where F_j is the scattering amplitude of shape J if it were centered at the origin. The phase shift accounts for the displacement from the origin. The scattering intensity can then be calculated as

$$I(\mathbf{q}) = \sum_J \sum_K F_J(\mathbf{q})F_K^*(\mathbf{q})\exp(i\mathbf{q}\cdot\Delta\mathbf{r}) \tag{8}$$

where * denotes the complex conjugate, and $\Delta\mathbf{r}$ is the separation between shape J and K. We assume that each shape comes from a distribution with a well-defined mean. The scattering amplitude for shape J can be rewritten as $F_J = \langle F\rangle + \delta F_J$, where δF_J denotes the deviation of the scattering amplitude for shape J away from the average. The intensity

is then

$$\begin{aligned} I(\mathbf{q}) &= |\langle F(\mathbf{q})\rangle|^2 S(\mathbf{q}) + \sum_J \sum_K \delta F_J \delta F_K^* \exp(i\mathbf{q}\cdot\Delta\mathbf{r}) \\ &= I_m(\mathbf{q}) + I_d(\mathbf{q}) \end{aligned} \tag{9}$$

where

$$S(\mathbf{q}) = \sum_J \sum_K \exp(i\mathbf{q}\cdot\Delta\mathbf{r}) \tag{10}$$

$I_m(\mathbf{q})$ and $I_d(\mathbf{q})$ are the mean scattering located at the Bragg peaks and the diffuse scattering, respectively.

The structure factor, $S(\mathbf{q})$ is approximated as a series of Gaussian peaks located at $q_x = 2\pi n/P$ where P is the pattern pitch. The height and width of these Gaussian peaks (A_1 and A_2, respectively) are fit parametrically from the experimental data.

$$S(\mathbf{q}) = A_1 \sum_{n=-\infty}^{\infty} \exp\left[\frac{-\left(q_x - \frac{2\pi n}{P}\right)^2}{2A_2^2}\right] \tag{11}$$

Additionally, the diffuse scattering, I_d, is fit parametrically prior to running simulations to extract an appropriate background baseline to be added to I_m when comparing to experimental data. It is fit to a curve of the form

$$I_d = \frac{B_0}{1 + (B_1 q_x)^{B_2}} + B_3 \tag{12}$$

The mean scattering, I_m, is what is investigated using simulations. A further simplification is made to the equation by segmenting the system in the y direction into pieces of length λ that are small enough to be approximately constant.[46] In this case, the scattering amplitude is then

$$F(\mathbf{q}) = \sum_m \lambda F_{2\mathrm{D}}(q_x, q_z)\mathrm{sinc}(0.5\lambda q_y)\exp(iq_y\Delta y_m) \tag{13}$$

where $F_{2\mathrm{D}}$ is the form factor of the 2D projection of each shape onto the xz plane. In our

experiments, we focus specifically on the plane where $q_y = 0$. Since we only consider data in this plane, Equation 13 can be further simplified to

$$|\langle F(\mathbf{q})\rangle|^2 = n^2\lambda^2|\langle F_{\mathrm{2D}}(q_x, q_z)\rangle|^2 \tag{14}$$

The 2D form factor, F_{2D} is calculated from simulations in a series of steps designed to eliminate gridding artifacts. First, the polymer density field over a small length in the y direction projected onto the xz plane, providing a 2D density field, and segmented into a binary representation of PS and PMMA domains using $\phi_A = \phi_B$ as a boundary. An illustration for how these domains are defined is given in Supporting Fig. 1. The 2D projection and binary representation effectively decouples the domain shape and the diffuse interface. The Fourier transform of the shapes can be calculated analytically,[30,47] while the diffuse interface is accounted for through multiplication by a smoothing function $H(q_x, q_z)$. As a first approximation we chose to employ two independent functions along each direction described by $H(q, \Delta_a) = (\pi q \Delta_a/4)\mathrm{csch}(\pi q \Delta_a)$.[10] Therefore

$$F_{\mathrm{2D}}(q_x, q_z) = F_{\mathrm{poly}}(q_x, q_z)H_x(q_x, \Delta_{a,x})H_z(q_z, \Delta_{a,z}) \tag{15}$$

The Monte Carlo simulation samples from the equilibrium ensemble, so the average form factor, $\langle F_{\mathrm{2D}}(\mathbf{q})\rangle$ is calculated by averaging $F_{\mathrm{2D}}(q_x, q_z)$ throughout the simulation to capture the appropriate structural fluctuations and variations that would be seen throughout a DSA film.

The calculated scattering is then compared to the experimental data. A fitness function for judging the closeness of the comparison is defined as

$$f = \sum_{\text{data points}} \left(\log(I_{\mathrm{exp}}) - \log(I_{\mathrm{sim}})\right)^2 \tag{16}$$

The logarithm of the intensity was selected to capture all features of the intensity profile

across six orders of magnitude. This fitness function is used within the Covariance Matrix Adaptation Evolution Strategy (CMA-ES)[20] to optimize the simulation input parameters until a suitable morphology has been reached.

One advantage of this type of analysis is that line edge roughness (LER) and line width roughness (LWR) can be calculated concurrently with the form factors.

Line Edge Roughness Calculations

As was stated in the previous section, the scattering is calculated by averaging the form factor of an ensemble of instantaneous morphologies during the Monte Carlo simulation. Each instantaneous density profile can be considered as a randomly selected 2D cross section from a unit cell. Statistical information about the interface location can be found from sampling sufficiently from these cross sections. In particular, measurements of the line edge roughness (LER) and line width roughness (LWR) along the lamella can be calculated. The LER and LWR reported in the main body of the paper were calculated from isocontours extracted from the simulations. The contour lines represented the center of the PS-PMMA interface. Calculations were performed on these isocontour lines at all film depths to determine the standard deviation in interface location and domain width, providing σ for LER and LWR, respectively as both a function of location over the pattern (x) and film depth (z).

Predictive interface fluctuation calculations for the samples not presented in the main text are shown in Supporting Fig. 2. These results were calculated using the same process as outlined above.

Acknowledgement

The experimental characterization of the samples considered here and the development of the evolutionary computation approach described here were supported by award 70NHNB14H012 from the U.S. Department of Commerce, National Institute of Standards and Technology, as part of the Center for Hierarchical Materials Design (CHiMaD). The development of the TICG model used here to describe copolymers was supported by the Department of Energy (DOE), Office of science, Basic Energy Sciences (BES), Materials Science and Engineering. The development of fast software for on-the-fly analysis of scattering data was supported by DOES, BES, Materials Science and Engineering through (MICCoM). This research used resources at beam line 11.0.1.2 at the Advanced Light Source, a U.S. Department of Energy Office of Science user facility under Contract No. DE-AC02-05CH11231. This research also used resources at beam line 8-ID-E at the Advanced Photon Source and the cleanroom and electron microscopy resources at the Center for Nanoscale Materials, which are U.S. Department of Energy Office of Science user facilities operated by Argonne National Laboratory under Contract No. DE-AC02-06CH11357.

References

(1) Ruiz, R.; Kang, H.; Detcheverry, F. A.; Dobisz, E.; Kercher, D. S.; Albrecht, T. R.; de Pablo, J. J.; Nealey, P. F. Density multiplication and improved lithography by directed block copolymer assembly. *Science* **2008**, *321*, 936–939.

(2) Stoykovich, M. P.; Müller, M.; Kim, S.; Solak, H.; Edwards, E.; de Pablo, J.; Nealey, P. Directed assembly of block copolymer blends into nonregular device-oriented structures. *Science* **2005**, *308*, 1442.

(3) Bita, I.; Yang, J. K.; Jung, Y. S.; Ross, C. A.; Thomas, E. L.; Berggren, K. K.

Graphoepitaxy of self-assembled block copolymers on two-dimensional periodic patterned templates. *Science* **2008**, *321*, 939–943.

(4) Yang, J. K.; Jung, Y. S.; Chang, J.-B.; Mickiewicz, R.; Alexander-Katz, A.; Ross, C.; Berggren, K. K. Complex self-assembled patterns using sparse commensurate templates with locally varying motifs. *Nature nanotechnology* **2010**, *5*, 256–260.

(5) Cheng, J. Y.; Sanders, D. P.; Truong, H. D.; Harrer, S.; Friz, A.; Holmes, S.; Colburn, M.; Hinsberg, W. D. Simple and Versatile Methods To Integrate Directed Self-Assembly with Optical Lithography Using a Polarity-Switched Photoresist. *ACS Nano* **2010**, *4*, 4815–4823, PMID: 20731456.

(6) Hu, T.; Jones, R. L.; Wu, W.-l.; Lin, E. K.; Lin, Q.; Keane, D.; Weigand, S.; Quintana, J. Small angle x-ray scattering metrology for sidewall angle and cross section of nanometer scale line gratings. *Journal of Applied Physics* **2004**, *96*, 1983–1987.

(7) Jones, R. L.; Hu, T.; Lin, E. K.; Wu, W.-L.; Kolb, R.; Casa, D. M.; Bolton, P. J.; Barclay, G. G. Small angle x-ray scattering for sub-100 nm pattern characterization. *Applied physics letters* **2003**, *83*, 4059–4061.

(8) Renaud, G.; Lazzari, R.; Leroy, F. Probing surface and interface morphology with grazing incidence small angle X-ray scattering. *Surf. Sci. Rep.* **2009**, *64*, 255–380.

(9) Sunday, D. F.; Hammond, M. R.; Wang, C.; Wu, W.; Delongchamp, D. M.; Tjio, M.; Cheng, J. Y.; Pitera, J. W.; Kline, R. J. Determination of the Internal Morphology of Nanostructures Patterned by Directed Self Assembly. *ACS Nano* **2014**, *8*, 8426–8437, PMID: 25075449.

(10) Stein, G. E.; Liddle, J. A.; Aquila, A. L.; Gullikson, E. M. Measuring the structure of epitaxially assembled block copolymer domains with soft X-ray diffraction. *Macromolecules* **2010**, *43*, 433–441.

(11) Perera, G. M.; Wang, C.; Doxastakis, M.; Kline, R. J.; Wu, W.-l.; Bosse, A. W.; Stein, G. E. Directed self-assembly of lamellar copolymers: effects of interfacial interactions on domain shape. *ACS Macro Letters* **2012**, *1*, 1244–1248.

(12) Doxastakis, M.; Suh, H. S.; Chen, X.; Delgadillo, P. A. R.; Wan, L.; Williamson, L.; Jiang, Z.; Strzalka, J.; Wang, J.; Chen, W. e. a. Grazing-incidence small angle x-ray scattering studies of nanoscale polymer gratings. SPIE Advanced Lithography. 2015; pp 94241N–94241N.

(13) Suh, H. S.; Chen, X.; Rincon-Delgadillo, P. A.; Jiang, Z.; Strzalka, J.; Wang, J.; Chen, W.; Gronheid, R.; de Pablo, J. J.; Ferrier, N.; Doxastakis, M.; Nealey, P. F. Characterization of the shape and line-edge roughness of polymer gratings with grazing incidence small-angle X-ray scattering and atomic force microscopy. *Journal of Applied Crystallography* **2016**, *49*.

(14) Tsai, H.; Pitera, J. W.; Miyazoe, H.; Bangsaruntip, S.; Engelmann, S. U.; Liu, C.-C.; Cheng, J. Y.; Bucchignano, J. J.; Klaus, D. P.; Joseph, E. A. e. a. Two-dimensional pattern formation using graphoepitaxy of PS-b-PMMA block copolymers for advanced FinFET device and circuit fabrication. *ACS nano* **2014**, *8*, 5227–5232.

(15) Schmid, G.; Farrell, R.; Xu, J.; Park, C.; Preil, M.; Chakrapani, V.; Mohanty, N.; Ko, A.; Cicoria, M.; Hetzer, D. e. a. Fabrication of 28nm pitch Si fins with DSA lithography. SPIE Advanced Lithography. 2013; pp 86801F–86801F.

(16) Liu, C.-C.; Thode, C. J.; Delgadillo, P. A. R.; Craig, G. S.; Nealey, P. F.; Gronheid, R. Towards an all-track 300 mm process for directed self-assembly. *Journal of Vacuum Science & Technology B* **2011**, *29*, 06F203.

(17) Liu, C.-C.; Ramírez-Hernández, A.; Han, E.; Craig, G. S. W.; Tada, Y.; Yoshida, H.; Kang, H.; Ji, S.; Gopalan, P.; de Pablo, J. J.; Nealey, P. F. Chemical Patterns for

Directed Self-Assembly of Lamellae-Forming Block Copolymers with Density Multiplication of Features. *Macromolecules* **2013**, *46*, 1415–1424.

(18) Delgadillo, P. A. R.; Gronheid, R.; Thode, C. J.; Wu, H.; Cao, Y.; Neisser, M.; Somervell, M.; Nafus, K.; Nealey, P. F. Implementation of a chemo-epitaxy flow for directed self-assembly on 300-mm wafer processing equipment. *Journal of Micro/Nanolithography, MEMS, and MOEMS* **2012**, *11*, 031302–1.

(19) Williamson, L. D.; Seidel, R. N.; Chen, X.; Suh, H. S.; Rincon Delgadillo, P.; Gronheid, R.; Nealey, P. F. Three-tone Chemical Patterns for Block Copolymer Directed Self-Assembly. *ACS applied materials & interfaces* **2016**,

(20) Khaira, G. S.; Qin, J.; Garner, G. P.; Xiong, S.; Wan, L.; Ruiz, R.; Jaeger, H. M.; Nealey, P. F.; de Pablo, J. J. Evolutionary optimization of directed self-assembly of triblock copolymers on chemically patterned substrates. *ACS Macro Letters* **2014**, *3*, 747–752.

(21) Detcheverry, F. A.; Kang, H.; Daoulas, K. C.; Müller, M.; Nealey, P. F.; de Pablo, J. J. Monte Carlo simulations of a coarse grain model for block copolymers and nanocomposites. *Macromolecules* **2008**, *41*, 4989–5001.

(22) Detcheverry, F. A.; Liu, G.; Nealey, P. F.; de Pablo, J. J. Interpolation in the Directed Assembly of Block Copolymers on Nanopatterned Substrates: Simulation and Experiments. *Macromolecules* **2010**, *43*, 3446–3454.

(23) Hur, S.-M.; Thapar, V.; Ramírez-Hernández, A.; Khaira, G.; Segal-Peretz, T.; Rincon-Delgadillo, P. A.; Li, W.; Müller, M.; Nealey, P. F.; de Pablo, J. J. Molecular pathways for defect annihilation in directed self-assembly. *Proceedings of the National Academy of Sciences* **2015**, *112*, 14144–14149.

(24) Fredrickson, G. *The equilibrium theory of inhomogeneous polymers*; Oxford University Press, USA, 2006.

(25) Matsen, M. W. The standard Gaussian model for block copolymer melts. *Journal of Physics: Condensed Matter* **2001**, *14*, R21.

(26) Qin, J.; Khaira, G. S.; Su, Y.; Garner, G. P.; Miskin, M.; Jaeger, H. M.; de Pablo, J. J. Evolutionary pattern design for copolymer directed self-assembly. *Soft Matter* **2013**, *9*, 11467–11472.

(27) Miskin, M. Z.; Khaira, G.; de Pablo, J. J.; Jaeger, H. M. Turning statistical physics models into materials design engines. *Proceedings of the National Academy of Sciences* **2016**, *113*, 34–39.

(28) Hannon, A. F.; Sunday, D. F.; Windover, D.; Kline, R. J. Advancing x-ray scattering metrology using inverse genetic algorithms. *Journal of Micro/Nanolithography, MEMS, and MOEMS* **2016**, *15*, 034001–034001.

(29) Perkins, S. J.; Wright, D. W.; Zhang, H.; Brookes, E. H.; Chen, J.; Irving, T. C.; Krueger, S.; Barlow, D. J.; Edler, K. J.; Scott, D. J.; Terrill, N. J.; King, S. M.; Butler, P. D.; Curtis, J. E. Atomistic modelling of scattering data in the Collaborative Computational Project for Small Angle Scattering (CCP-SAS). *Journal of Applied Crystallography* **2016**, *49*.

(30) Lee, S.-W.; Mittra, R. Fourier transform of a polygonal shape function and its application in electromagnetics. *Antennas and Propagation, IEEE Transactions on* **1983**, *31*, 99–103.

(31) Lazzari, R. IsGISAXS: a program for grazing-incidence small-angle X-ray scattering analysis of supported islands. *Journal of Applied Crystallography* **2002**, *35*, 406–421.

(32) Mahadevapuram, N.; Strzalka, J.; Stein, G. E. Grazing-incidence transmission small angle X-ray scattering from thin films of block copolymers. *Journal of Polymer Science Part B: Polymer Physics* **2013**, *51*, 602–610.

(33) Lee, B.; Park, I.; Yoon, J.; Park, S.; Kim, J.; Kim, K.-W.; Chang, T.; Ree, M. Structural analysis of block copolymer thin films with grazing incidence small-angle X-ray scattering. *Macromolecules* **2005**, *38*, 4311–4323.

(34) Busch, P.; Rauscher, M.; Smilgies, D.-M.; Posselt, D.; Papadakis, C. M. Grazing-Incidence Small-Angle X-ray Scattering from thin polymer films with lamellar structures–the scattering cross section in the Distorted-Wave Born Approximation. *Journal of applied crystallography* **2006**, *39*, 433–442.

(35) Yan, M.; Gibaud, A. On the intersection of grating truncation rods with the Ewald sphere studied by grazing-incidence small-angle X-ray scattering. *Journal of Applied Crystallography* **2007**, *40*, 1050–1055.

(36) Wernecke, J.; Scholze, F.; Krumrey, M. Direct structural characterisation of line gratings with grazing incidence small-angle x-ray scattering. *Review of Scientific Instruments* **2012**, *83*, 103906.

(37) Hofmann, T.; Dobisz, E.; Ocko, B. Grazing incident small angle x-ray scattering: A metrology to probe nanopatterned surfaces. *Journal of Vacuum Science & Technology B: Microelectronics and Nanometer Structures Processing, Measurement, and Phenomena* **2009**, *27*, 3238–3243.

(38) Hlaing, H.; Lu, X.; Hofmann, T.; Yager, K. G.; Black, C. T.; Ocko, B. M. Nanoimprint-induced molecular orientation in semiconducting polymer nanostructures. *ACS nano* **2011**, *5*, 7532–7538.

(39) Wernecke, J.; Krumrey, M.; Hoell, A.; Kline, R. J.; Liu, H.-K.; Wu, W.-L. Traceable GISAXS measurements for pitch determination of a 25 nm self-assembled polymer grating. *Journal of Applied Crystallography* **2014**, *47*, 1912–1920.

(40) Russell, T. P.; Jr., R. P. H.; Seeger, P. A. Temperature dependence of the interaction

parameter of polystyrene and poly(methyl methacrylate). *Macromolecules* **1990**, *23*, 890–893.

(41) Segal-Peretz, T.; Winterstein, J.; Ren, J.; Biswas, M.; Liddle, J. A.; Elam, J. W.; Zaluzec, N.; Nealey, P. F. Metrology of DSA process using TEM tomography. SPIE Advanced Lithography. 2015; pp 94240U–94240U.

(42) Segal-Peretz, T.; Winterstein, J.; Doxastakis, M.; Ramírez-Hernández, A.; Biswas, M.; Ren, J.; Suh, H. S.; Darling, S. B.; Liddle, J. A.; Elam, J. W. e. a. Characterizing the three-dimensional structure of block copolymers via sequential infiltration synthesis and scanning transmission electron tomography. *ACS nano* **2015**, *9*, 5333–5347.

(43) Segal-Peretz, T.; Winterstein, J.; Biswas, M.; Liddle, J.; Elam, J. W.; Zaluzec, N.; Nealey, P. Staining Block Copolymers using Sequential Infiltration Synthesis for High Contrast Imaging and STEM tomography. *Microscopy and Microanalysis* **2015**, *21*, 611–612.

(44) Jiang, Z.; Li, X.; Strzalka, J.; Sprung, M.; Sun, T.; Sandy, A. R.; Narayanan, S.; Lee, D. R.; Wang, J. The dedicated high-resolution grazing-incidence X-ray scattering beamline 8-ID-E at the Advanced Photon Source. *Journal of synchrotron radiation* **2012**, *19*, 627–636.

(45) Ren, J.; Ocola, L. E.; Divan, R.; Czaplewski, D. A.; Segal-Peretz, T.; Xiong, S.; Kline, R. J.; Arges, C. G.; Nealey, P. F. Post-directed-self-assembly membrane fabrication for in situ analysis of block copolymer structures. *Nanotechnology* **2016**, *27*, 435303.

(46) Wang, C.; Jones, R. L.; Lin, E. K.; Wu, W.-L.; Rice, B. J.; Choi, K.-W.; Thompson, G.; Weigand, S. J.; Keane, D. T. Characterization of correlated line edge roughness of nanoscale line gratings using small angle x-ray scattering. *Journal of Applied Physics* **2007**, *102*, 024901.

(47) Chu, F.-L.; Huang, C.-F. On the calculation of the Fourier transform of a polygonal shape function. *Journal of Physics A: Mathematical and General* **1989**, *22*, L671.

Graphical TOC Entry